PERGAMON

International Journal of Heat and Mass Transfer 44 (2001) 3067–3080

International Journal of HEAT and MASS TRANSFER

www.elsevier.com/locate/ijhmt

Numerical investigation of transient buoyant flow in a room with a displacement ventilation and chilled ceiling system

S.J. Rees [a,*], J.J. McGuirk [b], P. Haves [c]

[a] School of Mechanical and Aerospace Engineering, Oklahoma State University, 218 Engineering North, Stillwater, OK 74074, USA
[b] Department of Automotive and Aeronautical Engineering, Loughborough University, Loughborough, Leicestershire LE11 3TU, UK
[c] Lawrence Berkley National Laboratory, 1 Cyclotron Road, Mailstop 90-3111, Berkeley, CA 94720, USA

Received 16 February 2000; received in revised form 25 October 2000

Abstract

The air flow in the office ventilation system known as displacement ventilation is dominated by a gravity current from the inlet and buoyant plumes above internal heat sources. Calculations of the flow and heat transfer in a typical office room have been made for this type of ventilation system used in conjunction with chilled ceiling panels. These calculations have been made in parallel with full size test chamber experiments. It has been found that with higher values of internal load (45 and 72 W m^{-2} of floor area) the flow becomes quasi-periodic in nature. Complex lateral oscillations are seen in the plumes above the heat sources which impinge on the ceiling and induce significant recirculating flows in the room. The frequency spectra of the transient calculations show good agreement with those of the experimental results. Comparison is also made between calculated mean room air speeds and temperature profiles and measured values.

1. Introduction

The work described here concerns a study of flow and heat transfer in a type of office ventilation system known as displacement ventilation, with supplementary cooling provided by a chilled ceiling. Experiments were carried out in an environmental test chamber equipped with this type of system, under a range of operating conditions. Numerical calculations of the room airflow and heat transfer were carried out in parallel with the experiments using the test chamber geometry and experimental boundary conditions.

The flow in this type of system differs from that of other types of ventilation systems in that the buoyancy forces are very significant. Other numerical studies of this type of system [1,2] have modeled the fluid as incompressible, treated buoyancy using the Boussinesq approximation, and used eddy diffusivity turbulence models with some success. These studies have, however, ignored transient effects.

For reasons discussed below, supplementary cooling by a chilled ceiling is necessary when dealing with larger room heat loads using a displacement ventilation system. Larger room heat loads imply a greater number of people and more items of electrical equipment, and hence a greater number of plumes generated in the room. When making calculations for smaller loads (<40 W m^{-2}), using a single heat source, preliminary work showed that it was possible to obtain a steady-state solution by using a false time-stepping procedure. However, when larger loads from four heat sources were modeled, no steady-state solution could be found and it was necessary to make a fully transient calculation. The results of these transient calculations showed a quasi-periodic variation in the flow field, which was also observed in the experiments. The results of these calculations are presented and discussed here.

2. Background

Conventional air distribution systems for office rooms employ slotted openings adjacent to either wall or ceiling surfaces with air supply velocities of the order of

* Corresponding author. Tel.: +1-405-744-5900; fax: +1-405-744-7873.
E-mail address: sjrees@okstate.edu (S.J. Rees).

0017-9310/01/$ - see front matter
PII: S0017-9310(00)00348-3

Nomenclature

C	turbulence model coefficient
C_p	specific heat capacity
g_i	gravitational acceleration vector
g	metric tensor
h	specific static enthalpy
I	total flux
k	turbulent kinetic energy
P	pressure
S	source term
t	time
T	temperature
U	mean velocity
x	distance in coordinate direction

Greek symbols

β	coefficient of thermal expansion
ε	turbulent kinetic energy dissipation rate
Γ	diffusion coefficient
μ	dynamic viscosity
ϕ	general independent variable
ρ	density
σ	Prandtl number

Subscripts

eff	effective
i, j	coordinate index
0	reference (density)
t	turbulent

3 m s^{-1} ($Re \sim 10\,000$). The intent in these systems is to produce wall jets that have sufficient momentum to travel most of the way across the ceiling before their mean velocity has decayed to that of the mean room velocity. The momentum of the jets and the entrainment of the room air into the jet promote a general recirculation pattern in the room. Heat and contaminants generated within the room therefore become well mixed in the recirculating room air.

The room air distribution system studied in this work is very different to conventional systems in several respects. Displacement ventilation systems seek to avoid any mixing of the air within the room and to rely on buoyancy forces to establish a movement of air from low to high level within the room. Rather than maintaining uniform air temperature and contaminant concentrations throughout most of the room, vertical gradients of both temperature and contaminant concentration are allowed to develop. The aim is that occupants are exposed to temperature and air-quality conditions that are close to the supply air conditions [3–5]. Displacement ventilation systems seek to achieve this by introducing the supply air at very low velocity near the floor at temperatures only a few degrees below the 'operating temperature' of the room (see Fig. 1). The Archimedes number at the inlet is typically of order one ($Re \sim 3000$) so that the cool air from the supply diffuser descends towards the floor in a short distance [6]. This flow forms a gravity current and is slightly warmed as it spreads over the floor surface.

Buoyant plumes develop around any warm object in a room such as people and electrical equipment. Air is entrained into the plumes from the air near the floor and also from the surrounding air in the lower part of the room. Each plume increases in size and flow rate with height until it reaches an upper zone, bounded by the ceiling, where there is some mixing [3]. In principle, there

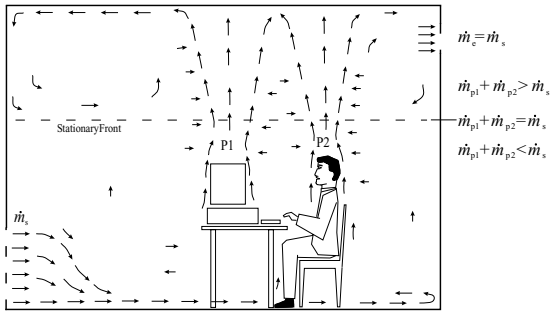

Fig. 1. The characteristic flow patterns in an office room with displacement ventilation.

is a height in the room at which the sum of the upward flow in the plumes is equal to the supply flow. As air is extracted from the upper layer of air at the same rate as the supply, continuity dictates that in stable conditions air in the upper layer does not fall below this height before being extracted [7]. The interface between the bottom of the mixed layer adjacent to the ceiling is referred to as the 'stationary front'.

It is this separation of the room air flow into a lower 'un-mixed' zone and an upper layer of mixed warm air that enables displacement ventilation to show advantages in air quality in the occupied zone compared to conventional mixing systems. The supply air can be introduced into the room at only one or two degrees below the operating temperature, giving such systems a thermodynamic advantage. This allows the refrigeration systems used to cool the air to be operated at a higher COP, or to be dispensed with altogether.

The effect of the transport of heat in the room to a layer of warm air near the ceiling is to produce a temperature gradient over most of the height of the room. Where displacement ventilation systems are used without

a chilled ceiling, there is a direct relationship between the overall temperature gradient and the heat gains in the room. There is also a well-known relationship between air temperature gradients and thermal comfort. Some authors suggest a maximum air temperature gradient of 2 K m^{-1} and others an overall head-to-foot difference of 3 K for acceptable thermal comfort. To stay within these guidlines therefore imposes a limit on the size of gains that can be dealt with by displacement ventilation systems. This limit is approximately 30 W m^{-2} (values between 20 and 40 W m^{-2} are suggested in the literature). Chilled ceilings are used to provide additional cooling in cases where the load is significantly greater.

3. Numerical method

The numerical model of room air flow is formulated from the incompressible form of the Navier–Stokes equations, together with an eddy viscosity turbulence model. The body forces of interest here are those due to buoyancy. These are dealt with using the Boussinesq approximation so that density changes are related to temperature difference by use of the thermal expansion coefficient, β. The body force term in the momentum equations then becomes $\rho_0\beta(T-T_0)g_i$, where ρ_0 and T_0 are the reference density and temperature, respectively. When the Boussinesq assumption and an eddy viscosity turbulence model are employed, the Reynolds-averaged Navier–Stokes equations can be expressed in Cartesian tensor notation as:

$$\frac{\partial(\rho_0 U_i)}{\partial x_i} = 0, \tag{1}$$

$$\frac{\partial(\rho_0 U_i)}{\partial t} + \frac{\partial(\rho_0 U_i U_j)}{\partial x_j} = -\frac{\partial P'}{\partial x_i} + \frac{\partial}{\partial x_j}\mu_{\text{eff}}\left(\frac{\partial U_i}{\partial x_j} + \frac{\partial U_j}{\partial x_i}\right) + \rho_0\beta(T-T_0)g_i + S_i, \tag{2}$$

with an effective viscosity μ_{eff} defined by $\mu_{\text{eff}} = \mu_t + \mu$ and the pressure modified so that

$$P' = P + \frac{2}{3}\rho_0 k - \rho_0 g. \tag{3}$$

The turbulence model used here is based on the two-equation eddy viscosity model of Launder and Spalding [8]. The equation used to model k is of the form:

$$\frac{\partial(\rho_0 k)}{\partial t} + \frac{\partial(\rho_0 U_j k)}{\partial x_j} - \frac{\partial}{\partial x_j}\left(\left(\mu + \frac{\mu_t}{\sigma_k}\right)\frac{\partial k}{\partial x_j}\right) = P_k + G - \rho_0\varepsilon, \tag{4}$$

where P_k is the production due to strain and is given by

$$P_k = \mu_t\left(\frac{\partial U_i}{\partial x_j} + \frac{\partial U_j}{\partial x_i}\right)\frac{\partial U_i}{\partial x_j}, \tag{5}$$

and G is the production due to buoyancy forces and is given by

$$G = \frac{\mu_{\text{eff}}}{\sigma_T}\beta g_i \frac{\partial T}{\partial x_i}. \tag{6}$$

In the high Reynolds number form of the epsilon equation used here, several terms are neglected on the basis of their small magnitude so that the resulting modeled epsilon equation is

$$\frac{\partial(\rho_0\varepsilon)}{\partial t} + \frac{\partial(\rho_0 U_j\varepsilon)}{\partial x_j} - \frac{\partial}{\partial x_j}\left(\left(\mu + \frac{\mu_t}{\sigma_\varepsilon}\right)\frac{\partial\varepsilon}{\partial x_j}\right) = C_{\varepsilon 1}\frac{\varepsilon}{k}P_k - C_{\varepsilon 2}\rho_0\frac{\varepsilon^2}{k}. \tag{7}$$

The model constants C_μ, $C_{\varepsilon 1}$, $C_{\varepsilon 2}$, σ_k and σ_ε have the values 0.09, 1.44, 1.92, 1.0 and 1.3, respectively.

The energy equation in the code used in this work [9] is formulated in terms of the static enthalpy, h. With a two-equation eddy viscosity model, such as that used here, the turbulent heat fluxes are modeled using the eddy diffusivity hypothesis so that the modeled Reynolds-averaged energy equation becomes

$$\frac{\partial(\rho_0 h)}{\partial t} + \frac{\partial(\rho_0 U_j h)}{\partial x_j} - \frac{\partial}{\partial x_j}\left(\frac{\lambda}{C_p} + \frac{\mu_t}{\sigma_H}\right)\frac{\partial h}{\partial x_j} = S_e, \tag{8}$$

where S_e is a source term that is used here for the introduction of heat at the location of internal heat sources. In view of the very small temperature range of the flow the energy equation is closed using the calorific equation of state $h = C_p T$, where C_p takes a constant value.

The governing equations of fluid flow and heat transfer are discretized using a finite-volume method on a structured, non-orthogonal boundary fitted grid. The approach to discretizing the equations on the boundary fitted mesh involves transforming the equations into computational space but making as much use of the physical grid information as possible. The governing equations are transformed into computational space as follows. The equations are first all expressed as a canonical convection–diffusion equation in tensor form:

$$\frac{\partial(\rho_0\phi)}{\partial t} + \frac{\partial}{\partial x^i}(\rho_0 U^i\phi) = \frac{\partial}{\partial x^i}\left(\Gamma\frac{\partial\phi}{\partial x^i}\right) + S. \tag{9}$$

This can be written in a more convenient form as

$$\frac{\partial(\rho_0\phi)}{\partial t} + \frac{\partial I^i}{\partial x^i} = S, \tag{10}$$

where I^i is the total convective and diffusive flux. It can be shown that the divergence of a vector can be related to its covariant (I^{ri}) and normal ($\hat{I}^i$) forms by the following:

$$\frac{\partial I^i}{\partial x^i} = \frac{1}{\sqrt{g}}\frac{\partial}{\partial\xi^i}\left(\sqrt{g}I^{ri}\right) = \frac{1}{\sqrt{g}}\frac{\partial\hat{I}^i}{\partial\xi^i}. \tag{11}$$

This relationship is used to transform the general equation (10) into computational space and express it in terms of the normal flux vectors so that

$$\sqrt{g}\frac{\partial(\rho_0\phi)}{\partial t}+\frac{\partial \hat{I}^i}{\partial \xi^i}=\sqrt{g}S, \tag{12}$$

and

$$\hat{I}^i=\sqrt{g}I^{ri}=\rho_0\hat{U}^i\phi-\sqrt{g}g^{ij}\Gamma\frac{\partial\phi}{\partial\xi^j}. \tag{13}$$

The governing equations can be seen to be of similar form when transformed into computational space in this way, except that the scalar diffusivity, Γ has been replaced by $\sqrt{g}g^{ij}\Gamma$, an anisotropic diffusivity. The term $\sqrt{g}g^{ij}$ and the normal velocities $\hat{U}^i$ can be calculated by making direct use of the geometric information from the boundary fitted grid – specifically the cell volumes and area vectors. Burns and Wilkes [10] comment that this approach gives better results on distorted grids than calculating the transformation parameters numerically, as in the approach discussed by Thompson et al. [11].

Central differencing has been employed to discretize all diffusive flux terms of the integrated equations. Two convection differencing schemes have been used, the first using hybrid differencing [12] to treat the convection terms of all equations, and the second employing a higher (second)-order upwind scheme to treat the convection terms of the momentum and energy equations, but retaining hybrid differencing of the turbulence equations. The temporal terms have been discretized using implicit first-order backward differencing in time. Pressure coupling is dealt with using the SIMPLEC algorithm [13]. The procedure adopted here to overcome the problems of pressure–velocity decoupling on co-located non-orthogonal meshes is the Rhie–Chow pressure smoothing procedure [14].

4. The experiments

The experiments were conducted in the Loughborough University Department of Civil and Building Engineering environmental test chamber. The chamber is of a size representative of a two-person office and has a net floor area of 16.7 m^2. It is not quite symmetrical, owing to a column part way along the south wall. The general arrangement is sketched in Fig. 2(a).

The displacement ventilation system supply was via a semi-cylindrical diffuser on the centerline of the shorter end wall of the test chamber. Extract was via a grille above the door at the other end of the room. The supply diffuser was constructed with a perforated metal face of square holes over a foam rubber sheet so that the open area is estimated to be 80% of the geometric area. The chilled ceiling was constructed from a proprietary system of metal tiles occupying 88% of the total ceiling area.

The heater batteries and cooling coil of the air supply for the displacement ventilation system were controlled such that the temperature of the air stream could be maintained at ±0.1 K when in heating mode and ±0.3 K when in cooling mode. The chilled ceiling water supply temperature could be controlled within a ±0.2 K band. The pump flow rate was high enough to ensure a temperature difference of ~2 K across the chilled ceiling panel system at full load and so minimize any temperature difference across the ceiling surface.

The primary air and wall surface temperature sensors were type 'T' copper–constantan thermocouples. The thermocouples used for air temperature measurement had the junction mounted within a short open-ended stainless steel tube to provide protection from longwave radiation. Eighteen sensors were mounted on a vertical stand to allow measurement of the vertical distribution of the room air temperature. Surface temperature thermocouples were distributed around the walls in seven vertical lines each of four sensors to allow measurement of vertical temperature profiles. Thirteen surface temperature thermocouples were installed on the chilled ceiling and six on the floor surface.

Calibration of the thermocouples was carried out using a constant temperature water bath and a reference mercury-in-glass thermometer. An ice-point reference system was used in taking measurements from the

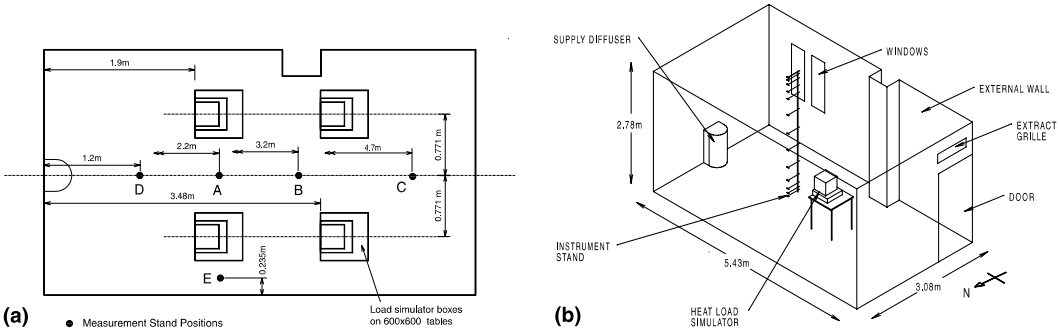

Fig. 2. The environmental test chamber apparatus. View (a) shows the general arrangement and (b) shows the layout of the room with four heat sources. Horizontal dimensions are measured from the left (east) wall.

Table 1
The main experimental parameters[a]

Test case	Load (W)	n (ac h^{-1})	T_{sw} (°C)	T_s (°C)	T_e (°C)
DC10	1200	5.0	16.0	19.8	25.9
DC11	800	5.0	16.0	19.0	22.6

[a] The temperatures tabulated are for the chilled water supply, air supply and air extract, respectively.

thermocouples. Testing of this ice-point-based measurement system before and after the experiments showed the air thermocouple measurements to be repeatable at ±0.17 K (absolute) and surface-to-air temperature difference measurements at ±0.25 K.

Air speed measurements were made using a Dantec 54N10 flow analyzer linked to a personal computer and connected to twelve 54R10 air flow transducers. The 54R10 air flow transducer is a hot-film omnidirectional air speed and temperature sensor designed for measuring room air flows within the velocity range 0.05–5.0 m s^{-1}. Air speed measurements were made by sampling the sensor signal twice a second over 2.5 min periods, followed by a 30 s delay, and recording the averaged values. The air flow transducers were mounted on the same vertical stand as the room air thermocouples. Air speed measurements were made for one of the test cases at a number of positions along the centerline of the room. These positions are noted as A–D in Fig. 2(b). An additional measurement was made at location E near to a side wall.

Internal loads were simulated in the test chamber using two sizes of cuboid boxes containing single domestic light bulbs of various wattages. When stacked these were intended to simulate a personal computer and monitor. The radiant component of the heat output from the load simulator boxes was measured at 50–55% by taking a series of radiometer readings over the box surfaces. (This information was used when assigning heat flux boundary conditions at the internal loads in the numerical model.) For the test cases reported here, four sets of boxes were placed on small square tables set symmetrically about the room centerline. The arrangement of the loads is also shown in Fig. 2(b).

Two of the 16 test chamber experiments carried out as part of this work [15] are used to define the boundary conditions in the transient calculations. These cases are denoted by DC10 and DC11 and had equal supply flow rates of 68.1 l s^{-1} (5 ac h^{-1}). Case DC11 had a moderate internal load of 800 W (47.9 W m^{-2} of floor area), and case DC10 a relatively high load of 1200 W (71.9 W m^{-2}). The principle experimental parameters are summarized in Table 1.

5. Results

Representation of the environmental test chamber geometry (Fig. 2) required the use of a boundary fitted mesh. This was necessary to accommodate the curved face of the supply diffuser at one end of the room. In the remainder of the room and in all vertical planes the mesh is orthogonal. The resulting mesh has 45 × 41 × 56 (103 320) cells and is illustrated in Fig. 3.

Initially a false time-stepping procedure was adopted in an attempt to calculate the steady-state solution to the flow. However, it was found that this method could not reduce the equation residuals adequately. Examination of the spatial distribution of the equation residuals did not reveal any particular regions in the flow that could be causing convergence difficulties. This situation could be explained by transient effects in the flow, such that a true steady state could no longer be defined. To examine this possibility a fully transient solution procedure was adopted.

When using the fully transient solution procedure, a spatially constant time step was applied without any further numerical underrelaxation. The convergence criteria were such that, at each time step, sufficient in-step iterations were carried out to ensure that the mass residual had fallen below 1% of the net flow through the room, and the enthalpy equation residual had fallen by

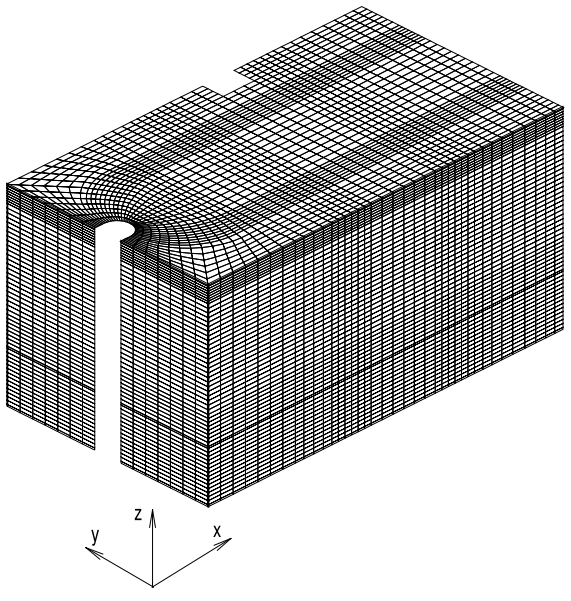

Fig. 3. The 45 × 41 × 56 mesh representing the environmental test chamber geometry.

four orders of magnitude. It was found that satisfactory convergence could be maintained with time steps of up to 3.0 s. Time steps of 3.0 s required 16 inner iterations per time step so that the procedure was computationally very expensive, progressing an order of magnitude slower than real time.

A calculation of the flow and temperature fields was made using two sets of experimental boundary conditions (noted above as DC10 and DC11). This was done by applying fixed temperature boundary conditions at the wall, ceiling and floor surfaces and fixed flux conditions at the four heat sources. When using these boundary conditions, an assumption has to be made about the fractional radiant output of the heat source and a value of 50% was used. The numbering of the heat sources and the corresponding plumes is indicated in Fig. 4.

To monitor the progress of the transient solution, a number of points were chosen at which the field values of each solution variable were recorded at each time step. Firstly, four points at high level in each plume were selected. The position of these monitoring points is shown in Fig. 4.

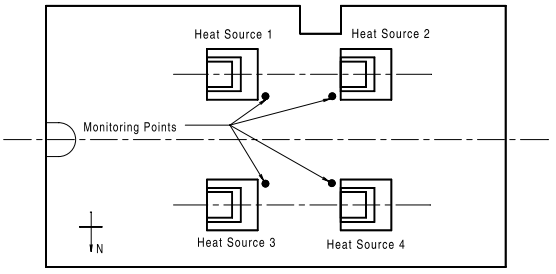

Fig. 4. A plan view of the test chamber showing the position of the plume monitoring points used in the calculations (at a height of 2.77 m) and the numbering of the heat sources.

The initial conditions of the calculations were zero velocity and a constant air temperature throughout. As the objective of the calculation was to find data representative of the measured conditions, data from the initial 4600 s of the calculation were disregarded. Examination of the data at the plume monitoring points for test case DC11 showed that after this time quasi-periodic fluctuations in the flow had evolved with a period of 450 s. These fluctuations continued and were observed in each solution variable. These data have been plotted in Fig. 5.

It was found that both the V velocity and temperature data obtained from the monitoring point in plume four were decaying. The calculation was therefore continued until a steady quasi-periodic variation was observed (from around 8000 s onwards, see Fig. 5). It may be noted that the amplitude of the fluctuations, particularly of the U and V velocities, is significant given that the maximum velocities near the base of the plumes are ~ 0.3 m s^{-1}.

A notable feature in the shape of the velocity and temperature signals at each monitoring point is that, within each period, there are two maxima and two corresponding minima (see Fig. 6). To analyze the fluctuating motion of the plumes further a set of animation data was generated on a vertical plane through the center of heat sources two and four (plane $x = 3.65$ m). Visualization of the temperature and velocity data at this plane showed that these plumes moved from side to side in the room, but plume four more so than plume two. The timing of the movement of plume four – either towards the north wall, upright or towards the room center

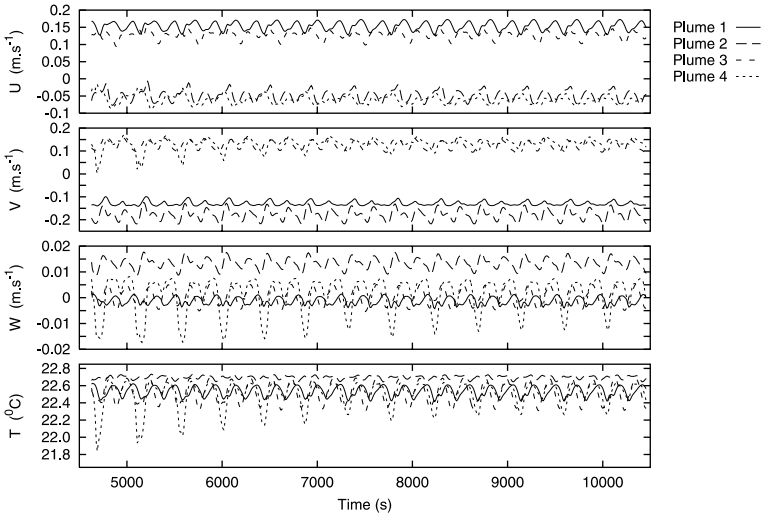

Fig. 5. The cyclic variations of the U, V and W velocity components and temperature at the four monitoring points during the progress of the transient calculation (case DC11).

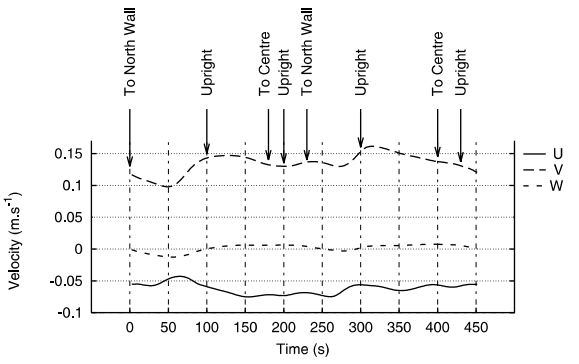

Fig. 6. Progress of the motion of plume four through one period of the observed steady periodic fluctuations (case DC11).

– was noted from the animated data. This information has been noted on a plot of the U, V and W velocity data for the plume four monitoring point in Fig. 6.

A notable feature of the observed motion of plume four is that the time taken to traverse from one side to the other differs at different parts of the period. For example, at ~200 s in the 450 s period this plume moves from its maximum deflection towards the room center, to its maximum northerly position over ~50 s, whereas, starting at time $t = 50$ s in the period it takes more than 100 s to complete the same movement in the opposite direction.

In order to find the cause, or driving forces producing this quasi-periodic motion two possibilities were first considered:

1. resonance in the plumes impinging on the ceiling (jet column instability);
2. vortex shedding caused by flow perpendicular to the axis of the plumes.

Impinging jets and plumes have been found to show instability under certain circumstances. By externally exciting a round free jet Crow and Champagne [16] found that lateral perturbations were amplified in the jet, the maximum amplitude occurring at a Strouhal number ($ST = fD_{\text{jet}}/U_{\text{jet}}$, where f is the frequency of the oscillations) of 0.3 and at a distance of 3.7 D_{jet} downstream. More recent research work [17] has established a range of Strouhal numbers between 0.24 and 0.51 where jet instability has been observed.

The feasibility of the existence of this phenomena in this case was examined by making an approximate calculation of the frequency given a target Strouhal number of 0.3. The resulting value of 0.2 Hz is two orders of magnitude higher than the fundamental frequency observed here (0.0022 Hz). It is therefore unlikely that this could be the principle mechanism driving the observed fluctuations.

A second possibility is that of a vortex shedding phenomena, in which the lateral flow through the room, from the inlet to exhaust, causes vortices to be generated as this flow crosses the region dominated by the plumes. In this case, the Strouhal number might be expected to be ~0.1 (and $ST = fD_{\text{plume}}/U_{\infty}$). If U_{∞} is estimated from the net flow through the room a frequency of 0.001Hz is obtained. Although lower than that observed this phenomena clearly leads to frequencies of the correct order of magnitude as those observed.

To analyze the oscillating motion of the plumes, further data were collected at the plume monitoring points over several periods. From these data, discrete Fourier transforms were calculated for each velocity component and temperature. The discrete Fourier transforms for plume four are shown in Fig. 7.

It can be seen that, in addition to the fundamental 2 mHz frequency there are further peaks in the spectrum at 4, 8 and 16 mHz. The largest peak occurs in the transformation of the temperature data at 8 mHz. These higher-order harmonics are a reflection of the complex nature of the fluctuations but do not necessarily suggest specific phenomena at these frequencies. The higher-frequency peaks may well arise from the asynchronous interaction of two or more phenomena.

To illustrate the features of the flow observable at each stage of the quasi-periodic motion of the plumes, the flow field has been plotted in vector form, at each of the eight steps identified in Fig. 6. The data have been plotted on a horizontal plane part way up the plumes ($z = 1.7$ m) and on a vertical plane through plumes two and four ($x = 3.65$ m). Vector plots projected on these planes are shown in Figs. 8–10.

The progression through the 450 s period can most easily be followed by reference to the motion of plume four which at time zero in the period – actually solution time 10 000 s – is positioned towards the north wall (the left and bottom wall in the section and plan views, respectively). At time 100 s plume four is upright and moves towards the center of the room by $t = 180$ s. This motion is reversed except on a shorter time scale between times 180 and 250 s. Plume four moves to an upright position again at $t = 300$ s and slowly towards the room center by 400 s. The motion is then quicker from this position to upright (430 s) and north again by 450 s.

Of the other plumes, plume three seems to move in the same direction as plume four, while plume one moves in the opposite direction. Plume two also moves in the opposite direction to plume four (so that they move towards the center of the room together, then apart) but by a much smaller amount.

Study of the flow vectors in these planes shows further details of the plume movement and its effect on the surrounding flow. Firstly, it can be seen that plume four, at each stage in the period, does neither penetrate so vigorously, nor impinge so strongly on the ceiling as plume two. It can also be seen that throughout the period there is no particular variation in the flow observable beneath

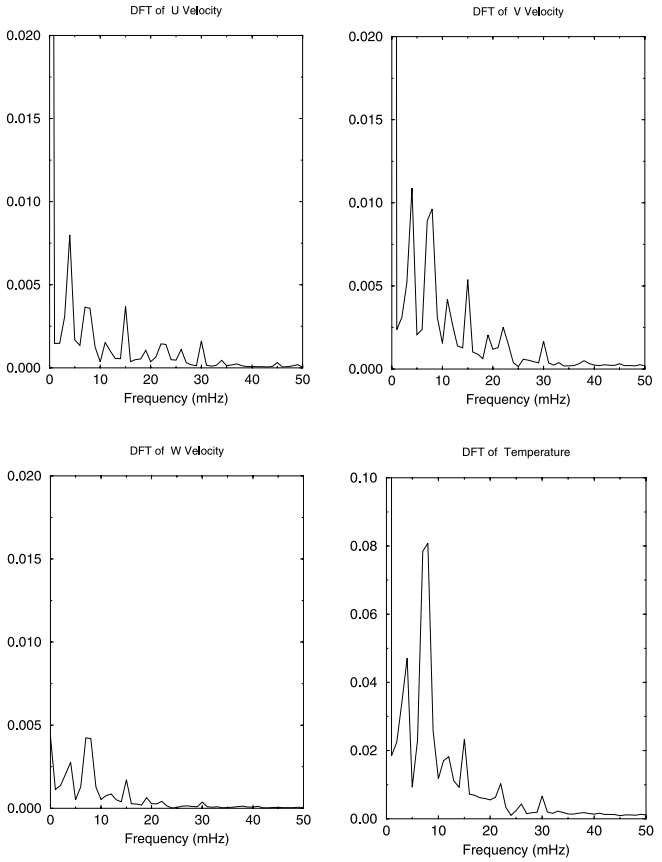

Fig. 7. Discrete Fourier transforms of the calculated U, V and W velocity components and temperature at the monitoring point in plume number 4 for case DC11.

the heat sources (0–0.7 m height), and that the velocities in this region are much lower in magnitude.

Between plume four and the north wall there is a noticeable recirculation pattern which seems most vigorous at 100 and 300 s when the plume is in an upright position. Between plumes two and four the wall jet flows from each plume impinge and this results in a swirling motion at high level. The recirculating flows surrounding the plumes exist over a height from 0.7 m and up to the ceiling and recirculate air to the very base of the plumes. This swirling motion varies in strength (again it seems most vigorous at 100 and 300 s) but always rotates in the same direction so that it acts in favor of the mean flow in plume two and against the mean flow of plume four. This probably accounts for the lack of penetration of plume four to the ceiling.

The vectors plotted on the horizontal plane in Figs. 8–10 show that the recirculating flow surrounding the plumes is not just a vertical movement but has a strong horizontal component. This is particularly noticeable between the north wall and the adjacent plumes where the flow is along the wall towards each corner of the room. This flow is also sufficient to impart a noticeable degree of swirl, at this height, to plumes three and four. A similar situation also exists around plume one, where there is a flow along the wall away from the column, and a corresponding swirl around the plume – although not so strongly as plumes three and four. This swirl around plume one varies more noticeably throughout the period and is hardly evident at 100 and 400 s. The flow at plume two is distorted and deflected from the axis of the heat source but there is little swirl or flow along the adjacent wall. In this case the motion of the plume seems to be stabilized by its proximity to the column.

The recirculating flow in the room that is entrained into the plumes is mostly drawn from the west and east walls where some vertical flow down the walls is evident. The fluctuations in the plume are evidently strong enough to induce fluctuations in this flow outside the plumes – compare the regions next to the diffuser at 250 and 400 s for example.

From the study of these data it appears that, with four heat sources in the test chamber, the flow entrained into the plumes is sufficiently large compared to the

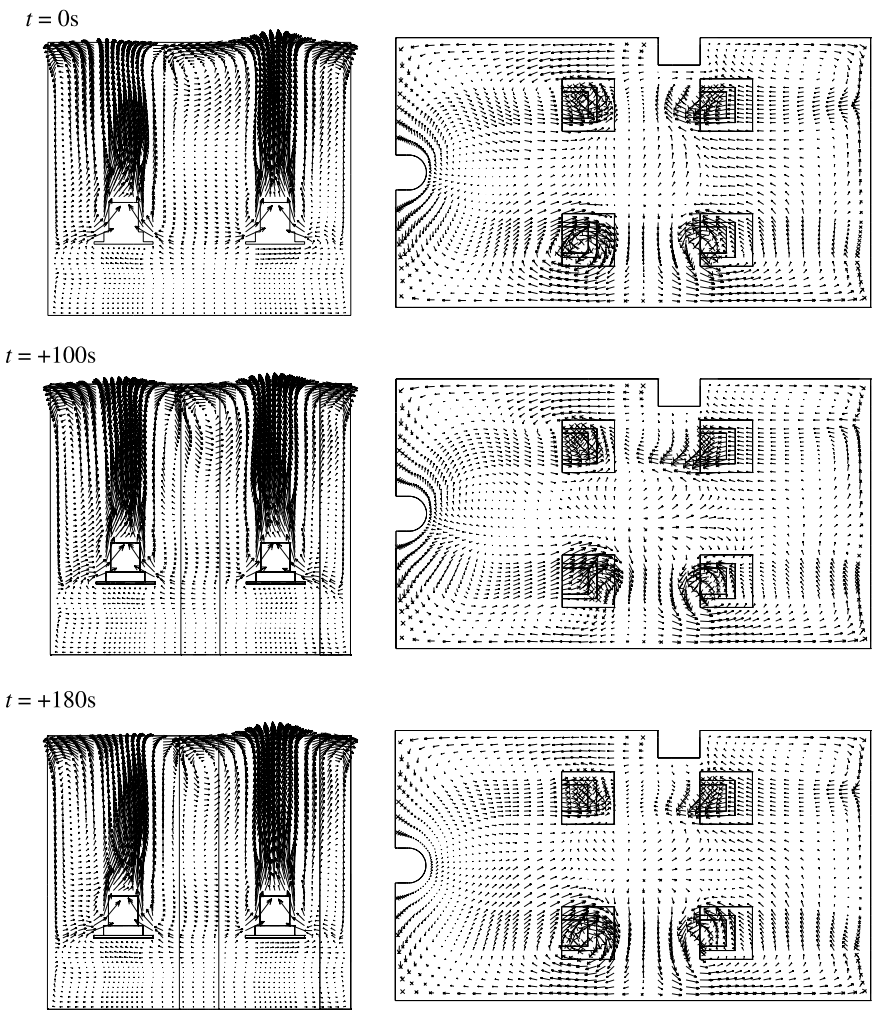

Fig. 8. Velocity vectors at plane $x = 3.65$ m (left) and at plane $z = 1.7$ m (right) at times 0, 100 and 180 s of the period.

supply flow that recirculating flows that fall to the base of the heat sources are generated in the upper region of the room. Furthermore, these recirculating flows, besides possessing the expected vertical velocity component, also have a significant horizontal component. These flows are strong enough to generate swirling effects in some locations.

It also appears that it is the interaction of the plumes with the recirculating flows and with each other that is causing the growth of the plumes to be unstable. There is some similarity between the observed flow and vortex shedding phenomena, in that, the recirculating flow around the plumes causes some swirling motion in the plumes and causes fluctuations with a frequency of the same order of magnitude. However, the results of the calculation do not show any separated vortices moving downstream.

Although the fluctuations in the calculated velocity and temperature at the plume monitoring points have been studied, no direct comparison with the experimental data was possible as no measurements were made at these points for case DC11. Some comparison with the experimental data was possible retrospectively however, at the temperature measuring positions on the room centerline. Calculated data have firstly been taken from six points equivalent to the position of six of the thermocouples. The calculated fluctuations in the temperature data at these points over several periods are shown in Fig. 11(a).

It can be seen that the fluctuations at low level in the room are very small in magnitude compared to those at high level. The largest amplitude fluctuations appear at 2.73 m in the calculated data. In the experiment temperatures were recorded over a period of approximately

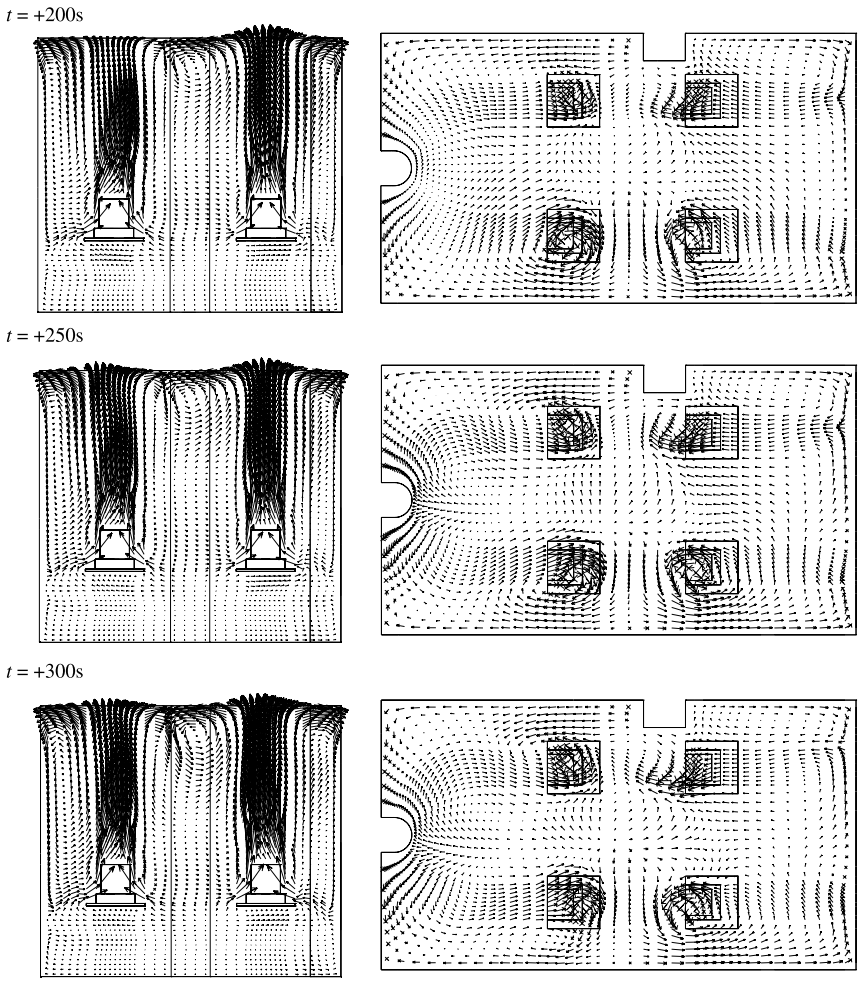

Fig. 9. Velocity vectors at plane $x = 3.65$ m (left) and at plane $z = 1.7$ m (right) at times 200, 250 and 300 s of the period.

45 min (fortunately long enough to include several of the predicted temperature fluctuation periods) with measurements made every second but averaged over 30 s before being logged. The recorded data are therefore at 30 s intervals and some of the fluctuations have been effectively filtered out. Nevertheless, fluctuations are present in the recorded experimental data from higher levels in the room.

A discrete Fourier transform has been calculated for the measured data from 2.73 m and is plotted in Fig. 11(b) along with the discrete Fourier transform of the equivalent calculated data. The Fourier transform from the calculated data shows harmonics at 5, 10, 15 and 18 mHz. These harmonics are at similar frequencies and magnitudes to those shown in the experimental data. As these fluctuations were not originally observed in the experimental data, this is a good example of how CFD predictions can be used to reveal physical phenomena in experiments that would have otherwise gone undetected.

Test case DC10 is similar to that of DC11 but each heat source has an output of 300 W rather than 200 W, giving a total load of 1200 W (equivalent to 71 W m^{-2} of floor area). It was particularly useful to make a calculation for this test case as velocity measurements had been made, along with temperature measurements, at a number of positions along the room centerline and can be compared with the calculated data.

In this case, it was found that steady periodic fluctuations developed in the CFD prediction at the four plume measuring positions after approximately 1800 s. The calculation was continued for a further 3200 s. The data from the plume monitoring positions showed a similar quasi-periodic form to the DC11 case, but with a shorter period of 383 s. The shortening of the period is not surprising in view of the increased momentum in each plume. Given that the supply flow rate is the same in case DC11, and the other boundary conditions are similar, the reduction in the period of the fluctuations suggests

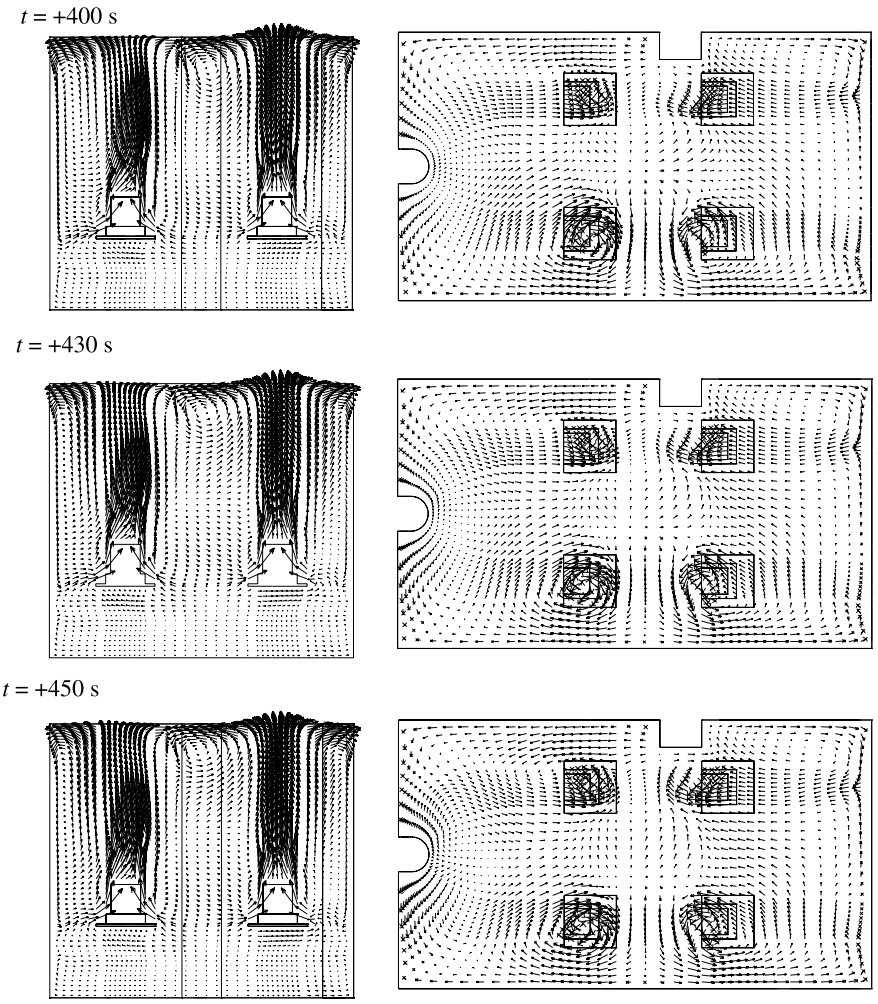

Fig. 10. Velocity vectors at plane $x = 3.65$ m (left) and at plane $z = 1.7$ m (right) at times 400, 430 and 450 s of the period.

that it is the momentum of the plumes that drives the recirculating flow and the fluctuations, rather than the negatively buoyant effects of the cold ceiling surfaces.

Temperature and velocity profiles were measured in the DC10 experiment along the room centerline at four different distances from the supply diffuser. To make a comparison with this temperature data the numerically calculated temperatures have been averaged over a whole period. The calculation was first made for this test case using hybrid differencing of the convective terms of all equations. The calculation was continued for several periods further using higher-order differencing and further temperature and velocity data extracted. The similarity of the predicted results using two different convection discretization schemes encourages the belief that the CFD predictions are close to grid independence.

The temperature profiles are compared at the four different positions in Fig. 12(a). From the floor up to a height of 1 m there is close agreement between calculated and experimental data except at $x = 4.7$ m (near the rear wall of the chamber) where the temperature near the floor is underpredicted. In the upper part of the room (above 1 m) the air temperature is overpredicted in the calculations by up to 0.8 K at $x = 3.2$ m. The experimental results also show a change in temperature gradient at approximately 1 m. This effect is shown in the calculated results but at a lower level of $\sim$0.75 m.

The mean air speed profiles are compared, at the four different positions, for test case DC10 in Fig. 12(b). As the experimental measurements were made with an omnidirectional probe, the numerically calculated velocities have been used to calculate air speeds, and then averaged over one whole period. Comparison of these results with the experimental data shows some of the same principle trends – namely that there are peaks in the air speed approaching the floor and ceiling, and

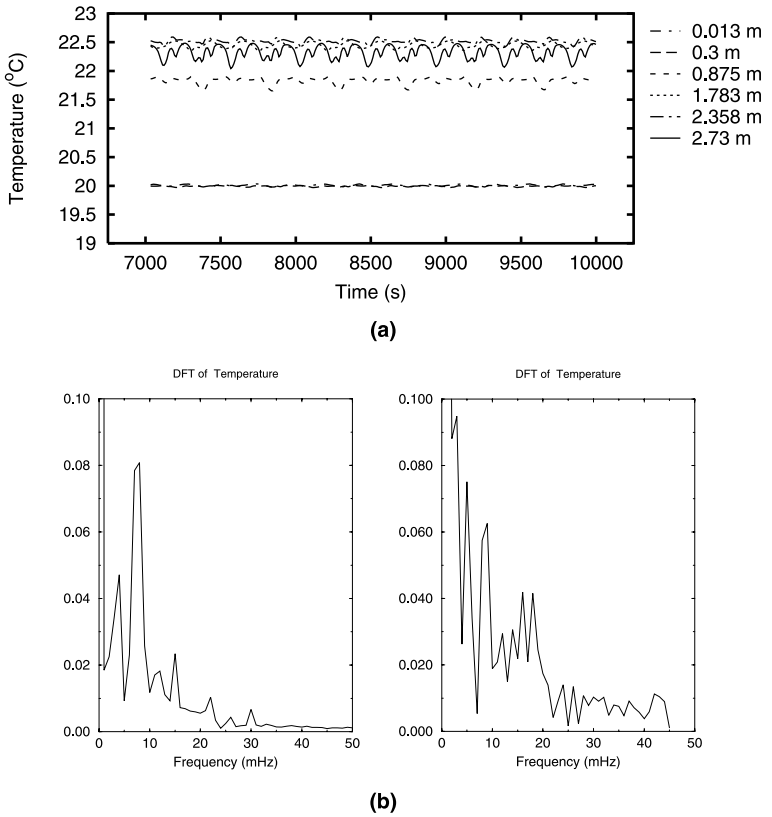

Fig. 11. Case DC11 temperature variations (a) calculated at different heights corresponding to the thermocouple positions, (b) comparison of discrete Fourier transforms of calculated and measured temperatures at height 2.73 m.

there is a local maximum part way up the height of the room.

Near the floor, the numerical results show a similar trend to the experimental data in that the speed immediately adjacent to the floor surface reduces with the distance from the supply diffuser. The agreement with the experimental data up to 0.5 m is generally very good. There is also good agreement above a height of 2 m except at a distance of $x = 4.7$ m. Where a local peak in air speed was measured consistently at ~1.1 m, the numerical results show peaks that are both lower in the room (~0.7 m) and lower in magnitude. At $x = 3.2$ m no particular peak part way up the height of the room is predicted at all. The difference in results from using the alternative differencing schemes is not great but higher-order upwinding could be said to offer slightly better results (see Fig. 12).

It is interesting that both the calculated changes in temperature gradient and the local maximum in the air speed are predicted to occur at a lower height in the room than that measured (~0.7 m compared with ~1.1 m measured). It seems likely that these features are associated with the bottom of the recirculating flows in the upper region of the room (i.e., the bottom of a well-mixed zone surrounding the plumes). If this is the case, then this would suggest that the depth of the upper well-mixed zone is overpredicted. This is consistent with the fact that the k–ε turbulence model is known to overpredict the spreading rate and entrainment factor of plumes [18,19], and hence the magnitude of the surrounding flow. For a given supply flow rate this would require a flow to be recirculated down to a lower level in the room than would actually occur.

6. Conclusions

Transient flow and heat transfer calculations have been made for a displacement ventilation and chilled ceiling system in parallel with test chamber experiments. The results of the calculations show that the flow is separated into two distinct regions of the room. These regions can be identified as firstly, near the floor and up to the height of the top of the supply diffuser, where the room flow is dominated by that from the diffuser, and secondly, above the top of the diffuser and up to the ceiling, where the flow is dominated by the plumes from the heat sources.

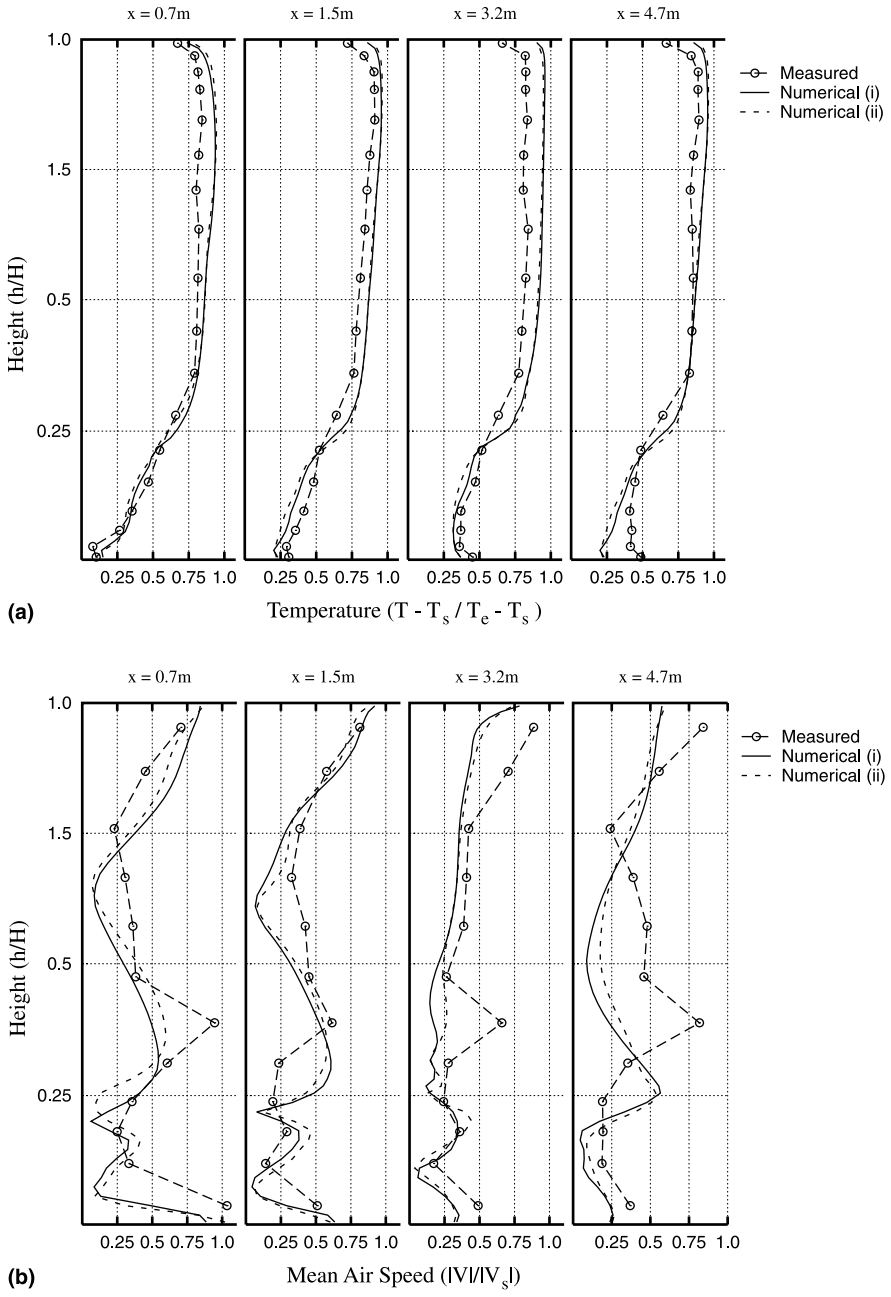

Fig. 12. Calculated temperature profiles (a) and air speed profiles (b) compared with experimental measurements for case DC10 at different distances (x) from the supply diffuser. The numerical results are for (i) hybrid differencing; (ii) higher-order upwind differencing. The temperature scale is normalized with the overall room temperature difference.

Complex quasi-periodic fluctuations in the room air flow have been observed in the predicted results. These fluctuations take the form of mainly lateral oscillations of the plumes above the heat sources. Some syncronization of the plume oscillations was observed, as the plumes tended to move to the center of the room together. However, complete symmetry of the motions was disturbed by the lack of symmetry in the room. These oscillations were found to have a Strouhal number in the range 0.16–0.21 with higher frequencies in the case of higher heat load, where the momentum in the plumes was greater.

The dynamic motion of the plumes seems to be due to the interaction between the plumes and the recirculating flows between the plumes, and between the plumes and the walls. It does not seem to be driven by the momentum associated with the inlet or any effects near the outlet from the room. The lateral movement of air in the recirculating flow surrounding the plumes is also significant enough to induce some swirling of the plumes.

Some of the predicted air temperature and velocity profiles from the transient calculations, when compared with experimental data, show evidence that the vertical extent of the recirculating flow in the upper region of the room is slightly overpredicted. This is most likely due to the known tendency of turbulence models such as the k–ε model used here to overpredict the entrainment into plumes.

The predictions of the fluctuations in the temperature field near the ceiling, induced by the motion of the plumes, have been shown to be very similar in magnitude and frequency to the fluctuations in the experimental data. This has demonstrated how numerical methods can be used to make predictions of the presence of phenomena in experiments that would be otherwise unobserved.

Acknowledgements

This work was funded jointly by British Gas plc, EA Technology, the Ove Arup Partnership and Loughborough University.

References

[1] T.V. Jacobsen, P.V. Neilsen, Numerical modelling of thermal environment in a displacement-ventilated room, in: Proceedings of the 'Indoor Air '93', Helsinki, Finland, vol. 5, 1993, pp. 301–306.
[2] Y. Li, L. Fuchs, M. Sandberg, Numerical prediction of airflow and heat-radiation in a room with displacement ventilation, Energy Build. 20 (1993) 27–43.
[3] E. Skåret, Displacement ventilation, in: Proceedings of the ROOMVENT-87, Stockholm, Sweden, vol. 4a, 1987.
[4] P.J. Jackman, Displacement ventilation, in: Proceedings of the CIBSE National Conference, Canterbury, 1991, pp. 364–380.
[5] P. Jackman, Displacement ventilation, Technical Memorandum 2/90, BSRIA, Bracknell, Berkshire, 1990, p. 36.
[6] M. Sandberg, S. Holmberg, Spread of supply air from low-velocity air terminals, in: Proceedings of the ROOMVENT-90, Oslo, Norway, 1990.
[7] P. Linden, G. Lane-Serff, D. Smeed, Emptying filling boxes: the fluid mechanics of natural ventilation, J. Fluid Mech. 212 (1990) 309–335.
[8] B. Launder, D. Spalding, The numerical computation of turbulent flow, Comput. Meth. Appl. Mech. Eng. 3 (1974) 269–289.
[9] CFDS. CFX-FLOW3D Release 4.1 User Guide. AEA Technology, Computational Fluid Dynamics Services, Harwell, Didcot, Oxfordshire, 1996.
[10] A. Burns, N. Wilkes, A finite difference method for the computation of fluid flows in complex three dimensional geometries, Technical Report AERE-R 12342, Atomic Energy Authority, Harwell, UK, 1987.
[11] J. Thompson, Z. Warsi, C. Mastin, Boundary-fitted coordinate systems for numerical solution of partial differential equations, J. Comput. Phys. 47 (1982) 1–108.
[12] D. Spalding, A novel finite difference formulation for differential expressions involving both first and second derivatives, Int. J. Numer. Meth. Eng. 4 (1972) 551–559.
[13] J. Van Doormaal, G. Raithby, Enhancements of the simple method for predicting incompressible fluid flows, Numer. Heat Transfer 7 (1984) 147–163.
[14] C. Rhie, W. Chow, A numerical study of the turbulent flow past an isolated airfoil with trailing edge separation, AIAA J. 21 (11) (1982) 1525–1532.
[15] S.J. Rees, Modelling of displacement ventilation and chilled ceiling systems using nodal models, Ph.D. thesis, Loughborough University, 1998.
[16] S. Crow, F. Champagne, Orderly jet structure in jet turbulence, J. Fluid Mech. 48 (1971) 547–549.
[17] E. Gutmark, C. Ho, On the preferred modes and spreading rates of jets, Phys. Fluids 26 (1983) 2932–2938.
[18] V. Shankar, L. Davidson, E. Olsson, Displacement ventilation: calculation of the flow in vertical plumes, in: Procedings of the ROOMVENT-94, vol. 4, 1994, pp. 59–74.
[19] Q. Chen, T. Chao, Predicition of buoyant plume and displacement ventilation with different turbulence models, in: Procedings of ROOMVENT-96, 1996, pp. 787–792.